

# Construction of Dual-Active-Site Copper Catalyst Containing both Cu–N<sub>3</sub> and Cu–N<sub>4</sub> Sites

Yu Xiong, Shibin Wang, Wenxing Chen, Jian Zhang, Qiheng Li, Han-Shi Hu,\*  
Lirong Zheng,\* Wensheng Yan, Lin Gu, Dingsheng Wang,\* and Yadong Li

Clear recognition and rational construction of suitable active center for specific reaction is always of great significance in designing highly efficient catalysts. Herein, a dual-active-site copper catalyst (DAS-Cu) containing both Cu–N<sub>3</sub> and Cu–N<sub>4</sub> sites is reported. Such catalysts show extremely high catalytic performance (yield: up to 97%) toward oxyphosphorylation of alkenes, while catalysts with single active site (Cu–N<sub>3</sub> or Cu–N<sub>4</sub>) are chemically inert in this reaction. Combined with theoretical and experimental results, the different roles of two different Cu active sites in this reaction are further identified. Cu–N<sub>3</sub> site captures the oxygen and trigger further oxidizing process, while Cu–N<sub>4</sub> site provides moderate adsorption sites for the protection of phosphonyl radicals. This work deeply discloses the significant cooperated role with two single-atomic sites in one catalytic active center and brings up a valuable clue for the rational design of better-performing heterogeneous catalyst.

Recently, single atom catalysts (SAC) draw a lot of attentions from researchers, because such catalysts not only show excellent catalytic activities but also possess single atomically active centers which can be identified by advanced characterizations (aberration-corrected high-angle annular dark-field scanning transmission electron microscopy (AC-HAADF-STEM) images, extended X-ray absorption fine structure (EXAFS) curve fitting, density functional theory (DFT) modeling, etc.).<sup>[11–32]</sup> However, SACs containing the unitary active sites are also a hindrance to their further applications. On the one hand, some complex reactions require two or more active sites to activate substrates, while SACs are incompetent on these reactions. On the other hand, the synergistic effect of dual

or more active sites can also improve the catalytic properties of simple reactions.<sup>[3,33–41]</sup> For example, Zbořil and co-workers developed a novel strategy to synthesize mixed-valence single atom catalysts by partial reducing the metal atoms (Fe or Cu) coordinated on nitrile groups functionalized graphene and discovered that the synergistic effect of Cu(II) and Cu(I) is the essential part in the oxidative coupling reaction.<sup>[20,40]</sup> Xiao et al. developed FeCoN<sub>x</sub>/C catalysts and discovered that the triangle FeCoN<sub>5</sub>–OH sites show about 20 times the activity of FeN<sub>4</sub> sites in oxygen reduction reaction.<sup>[39]</sup> However, the novel strategies and potential

## 1. Introduction

Catalytic active centers are known as central characters in catalysis since Taylor introduced this concept for nearly 100 years.<sup>[1–5]</sup> Recognizing active centers clearly in catalysts is critical to comprehend the reaction mechanism and design new catalysts with high efficiency. Since a variety of surface sites (including crystal facets, edges, corners, terrace, steps, kinks, etc.) coexist in traditional nanosized catalysts, the real catalytic active centers of these catalysts can be hardly identified.<sup>[6–10]</sup>

Dr. Y. Xiong  
Department of Chemistry and Chemical Engineering  
Central South University  
Changsha 410083, China

Dr. Y. Xiong, S. Wang, W. Chen, J. Zhang, Q. Li, Prof. H.-S. Hu,  
Prof. D. Wang, Prof. Y. Li  
Department of Chemistry, Tsinghua University  
Beijing 100084, China  
E-mail: hshu@mail.tsinghua.edu.cn;  
wangdingsheng@mail.tsinghua.edu.cn

Dr. S. Wang  
Institute of Industrial Catalysis  
State Key Laboratory Breeding Base of Green-Chemical Synthesis  
Technology  
College of Chemical Engineering  
Zhejiang University of Technology  
Hangzhou 310032, China

 The ORCID identification number(s) for the author(s) of this article can be found under <https://doi.org/10.1002/smll.202006834>.

Prof. L. Zheng  
Beijing Synchrotron Radiation Facility  
Institute of High Energy Physics  
Chinese Academy of Sciences  
Beijing 100049, China  
E-mail: zhenglr@ihep.ac.cn

Prof. W. Yan  
National Synchrotron Radiation Laboratory  
University of Science and Technology of China  
Hefei 230029, China

Prof. L. Gu  
Beijing National Laboratory for Condensed Matter Physics  
Institute of Physics  
Chinese Academy of Sciences  
Beijing 100190, China

DOI: 10.1002/smll.202006834

applications of dual-sites catalysts and the cooperation mechanisms of dual or more sites are far from dug out.

$\beta$ -ketophosphonates are highly valuable compounds, which serve as important synthetic intermediates for pharmaceutical and show interesting biological properties.<sup>[42–44]</sup> Difunctionalizing alkenes with H-phosphonates in air is the most facile (one-pot) and environmental benign (carbon balance and green oxidant) synthetic strategies.<sup>[44,46]</sup> Three steps (oxidation, coupling, and hydrogen transfer) are involved in this strategy. Both H-phosphonates and dioxygen should be activated and thus the division cooperation of two active sites can highly accelerate this reaction. Therefore, constructing and designing efficient catalysts with dual active sites can help with the completion of the reaction. Moreover, the further identification of the synergistic effect for different active sites can deepen the understanding of reaction mechanisms and pave the way for rational designing of novel dual-active-site (DAS) catalysts.

Herein, we prepared DAS-Cu catalysts with both Cu–N<sub>3</sub> and Cu–N<sub>4</sub> active sites on nitrogen-doped carbon by pyrolyzing Cu complexes. Atomically dispersed Cu is distinguished by AC-HAADF-STEM and two different kinds of Cu active sites are determined by EXAFS analysis combined with Cu 2p and Cu L-inner level-valence-valence electron transition (LVV) X-ray photoelectron spectroscopy (XPS) spectra. We surprisingly discover that such catalysts show great catalytic performance in oxyphosphorylation reaction (up to 97% yield in only 2 h), while catalyst possessing Cu–N<sub>3</sub> sites is inert and catalyst containing Cu–N<sub>4</sub> sites only shows trace reactivity under the same condition. The reasonable structure model containing Cu–N<sub>4</sub> and Cu–N<sub>3</sub> sites for the DAS-Cu was constructed depending on EXAFS, XPS and near-edge X-ray absorption fine structure spectra (NEXAFS) spectra. DFT calculations combined with electron paramagnetic resonance (EPR) studies investigate the reaction mechanism and the synergistic effect of Cu–N<sub>3</sub> and Cu–N<sub>4</sub>. It is believed that this work brings new insights in designing effective catalysts with coherence effects from two single-atoms based active sites in one catalytic center.

## 2. Results and Discussion

The DAS-Cu catalyst was synthesized via pyrolyzing Cu complexes. Creatine is chosen as key ligand of Cu complexes, because creatine provides two different coordination sites (guanidyl and carboxylate groups). In the synthetic procedure, Cu(NO<sub>3</sub>)<sub>2</sub>, NaOH, and creatine are first mixed in water and the claret powders are gained by vaporizing the solvent. During this process, Cu atoms are coordinated with guanidyl or carboxylate groups respectively. DAS-Cu catalysts with different Cu active sites are obtained after the calcination of the as-obtained powders and etching of excessive Cu nanoparticles (see detailed procedure in the Experimental Section; Figure S1, Supporting Information). Transmission electron microscopy (TEM) (Figure S2, Supporting Information) and scanning electron microscopy (Figure S3, Supporting Information) images show the laminar structure of DAS-Cu. The broad peak at around 26.5° in powder X-ray diffraction pattern (Figure S4, Supporting Information) indicates the hexagonal graphitic structure in DAS-Cu.<sup>[47]</sup> scanning transmission electron microscopy (STEM) image manifests no observable nanoparticles or clusters

in the catalyst (Figure 1a; and Figure S5, Supporting Information). In Figure 1b, energy-dispersive X-ray (EDX) mappings of DAS-Cu denote that Cu, C, and N are homogeneously distributed in the nanosheets. From AC-HAADF-STEM image, we can identify the atomically dispersed Cu by Z-contrast (Figure 1c). The metal loading of DAS-Cu is as high as 4.6 wt% (certified by inductively coupled plasma optical emission spectroscopy (ICP-OES) analysis), which indicates a short interatomic distance of neighboring Cu atoms. The further Z-contrast analysis of Cu atoms (region 1 and region 2 in Figure 1c; more typical adjacent Cu atoms are cycled by wathet ellipse) shows that the distances of the adjacent Cu atoms are between 4 and 6 Å (Figure 1d).

In order to identify the atomic local structure of the independent Cu species, XAFS spectroscopy was carried out. From Figure 1e, we can see the Cu K-edge X-ray absorption near-edge structure (XANES) spectra of DAS-Cu with Cu foil, Cu<sub>2</sub>O, and CuO as references. According to the height of white line ( $H_w$ ) at 8996.5 eV and the energy of absorption edge ( $E_0$ ) at 8988.0 eV, the average oxidation state number of Cu atoms in DAS-Cu is situated between zero and two.<sup>[48,49]</sup> The Fourier-transformed  $k^3$ -weighted EXAFS spectrum of DAS-Cu (Figure 1f) displays only one main peak at 1.56 Å, which correspond to the first coordination shell of Cu–N, and no obvious Cu–Cu peaks (2.24 Å) are observed. Tiny peaks located at  $\approx$ 2–4 Å can be assigned to the peaks of the second or higher Cu–C coordination shell (Figure S6, Supporting Information). This result further confirms the sole presence of single atomic Cu species in DAS-Cu catalyst. We next performed the EXAFS curve fitting analysis to study the quantitative structural parameters of Cu atoms (Figure S7 and Table S1, Supporting Information). Cu atoms in DAS-Cu show an average coordination numbers of 3.3 and an average bond length of 1.94 Å. The data indicate that two different kinds of Cu atomic sites coexist in DAS-Cu (the inset of Figure S7 (Supporting Information) is the corresponding model of atomic structure), which is coordinated by three or four N atoms, respectively.

The existence of different Cu sites is also determined by both Cu 2p and Cu LVV XPS spectra. XPS survey spectrum is shown in Figure S8 (Supporting Information), suggesting that C, N, O, and Cu are the major components in DAS-Cu. The XPS spectrum of DAS-Cu in Cu 2p region is shown in Figure 2a. Two main features can be distinguished clearly, which indicates the coexistence of two different Cu species in DAS-Cu. The feature located at 932.4 and 952.2 eV can be attributed to Cu species with the valence state close to +1, while the other feature which located at 934.6 and 954.3 eV can be attributed to Cu(II).<sup>[50]</sup> The Cu LVV Auger spectrum also shows two deconvoluted peaks, which can be assigned to two different species (Figure 2b).<sup>[51]</sup> On the basis of XPS spectra and EXAFS analysis, we can identify that Cu–N<sub>3</sub> and Cu–N<sub>4</sub> sites coexist in DAS-Cu catalysts.

C 1s, N 1s, and O 1s XPS spectra combined with NEXAFS are carried out to further clarify the structure of DAS-Cu. C 1s XPS spectrum of DAS-Cu deconvolves into four main peaks (Figure 2c). The major peak at 284.8 eV can be identified as aromatic C=C bonds and weaker peaks can be certified as C-sp<sup>3</sup> (285.7 eV), C-oxide (286.6 eV) and aromatic N–C=N (288.1 eV) respectively, which indicate the 2D structure with some defects and vacancies.<sup>[52,53]</sup> In C K-edge NEXAFS spectrum, four resonances in  $\pi^*$  region are detected (Figure 2d). The resonances at 284.8, 285.6, and 287.8 eV are associated with  $1s \rightarrow \pi^*$  (C=C),

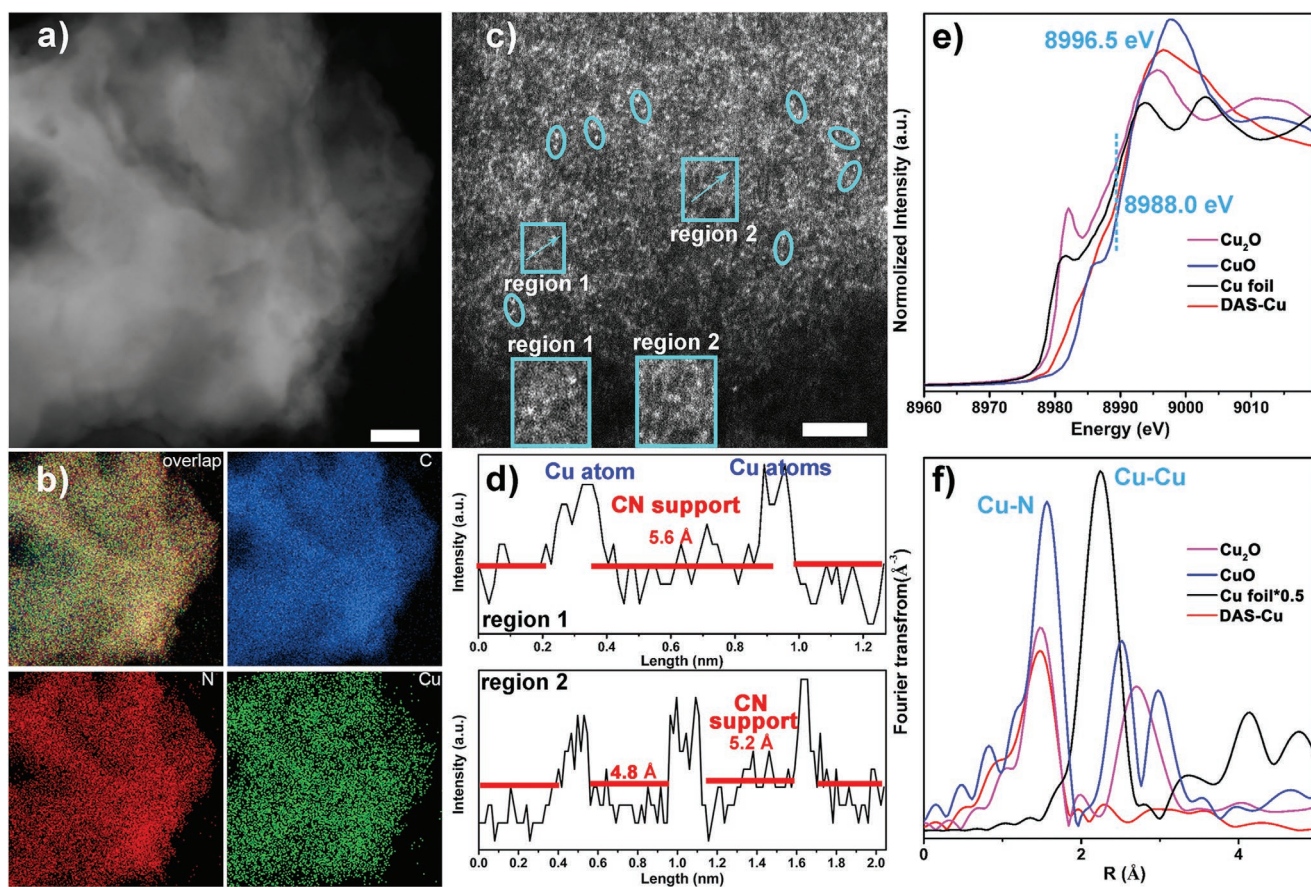


**Figure 1.** Characterizations of DAS-Cu. a,b) STEM image and corresponding EDX mappings of DAS-Cu, which show distributions of C (blue), N (red), Cu (green), respectively. Scale bar: 20 nm. c) AC-HAADF-STEM image of DAS-Cu; the enlarged image of region 1 and region 2 (inset). Scale bar: 5 nm. d) The corresponding Z-contrast analysis of region 1 and region 2. e,f) XANES spectra and Fourier transform EXAFS spectra of the DAS-Cu catalysts in comparison with Cu foil; Cu<sub>2</sub>O; CuO at the Cu K-edge.

$1s \rightarrow \pi^*$  (C=C=N) and  $1s \rightarrow \pi^*$  (N=C=N) transitions respectively, indicating the formation of nitrogen containing heteroarenes. The weaker resonance at 287.0 eV can be defined as the  $1s \rightarrow \pi^*$  (C=O), which suggest the carbonyl or carboxyl group at the edge of DAS-Cu. In  $\sigma^*$  region, the strong resonance at 292.2 eV can be assigned to  $1s \rightarrow \sigma^*$  (C-N) transition and the weaker resonance at 301.0 eV can be certified as  $1s \rightarrow \sigma^*$  (C=N; C=O; and C=C) transition.<sup>[54]</sup> Three deconvoluted peaks can be detected in N 1s XPS spectrum at 398.2, 399.6, and 400.7 eV, which are attributed to the pyridinic, graphitic, and pyrrolic nitrogen species, respectively (Figure 2e).<sup>[55]</sup> N K-edge NEXAFS spectrum of DAS-Cu shows three resonances in  $\pi^*$  region (399.5 eV for pyridinic N; 400.1 eV for pyrrolic N; 401.5 eV for graphitic N), which is coincidence with the N 1s XPS spectrum (Figure 2f). In  $\sigma^*$  region, the resonance at 407.1 eV can be defined as  $1s \rightarrow \sigma^*$  (C-N; C=N) transition.<sup>[56]</sup> Two main components are detected in O 1s XPS spectrum (Figure S9, Supporting Information), which can be identified as carbonyl group (533.5 eV) and absorbed oxygen (531.3 eV).<sup>[57]</sup> In conclusion, we can identify that Cu-N<sub>3</sub> and Cu-N<sub>4</sub> active sites are anchored on the 2D CN sheets with some pendant groups.

DFT calculations were performed to further understand the geometric and electronic structure of DAS-Cu. Previous experimental and theoretical studies have shown that single-

atomic sites supported on graphene are actually coordinated by pyridinic/pyrrolic nitrogen atoms, C atoms, or hybrid of C and N.<sup>[14,58-61]</sup> According to the research of Gao and co-workers,<sup>[62]</sup> single Cu atoms coordinated to pyridinic N with structures of Cu-N<sub>3</sub> site and Cu-N<sub>4</sub> site both exhibit higher stability in contrast to a hybrid coordination with C and N. Moreover, the experimental results of EXAFS, XPS, and NEXAFS analyses also strongly suggest that the Cu-N<sub>3</sub> and Cu-N<sub>4</sub> sites coexist in DAS-Cu. Therefore, these two isolated sites are used in the subsequent studies.

Though theoretical studies of structure for separate Cu-N<sub>4</sub><sup>[63]</sup> or Cu-N<sub>3</sub><sup>[64]</sup> have been reported, the synergistic catalysis with these two sites working together for highly efficient chemical reactions is rare. Since the distances between the separate Cu-N<sub>3</sub>/Cu-N<sub>4</sub> site are the crucial factor for the synergistic effect, the structures with different Cu-N<sub>3</sub>/Cu-N<sub>4</sub> distances are therefore thoroughly investigated. Their stabilities are measured by relative energies as well as average Cu binding energies. As shown in Figure 3a, the p-(6 × 6) graphene layer is employed and vacancy sites with different distances of Cu-N<sub>3</sub> and Cu-N<sub>4</sub> sites are proposed in three directions (a, b, c). Two vacancy sites are constructed along each of the three directions originated from the Cu-N<sub>4</sub> site. In total, six inequivalent DAS-Cu structures are constructed and the corresponding

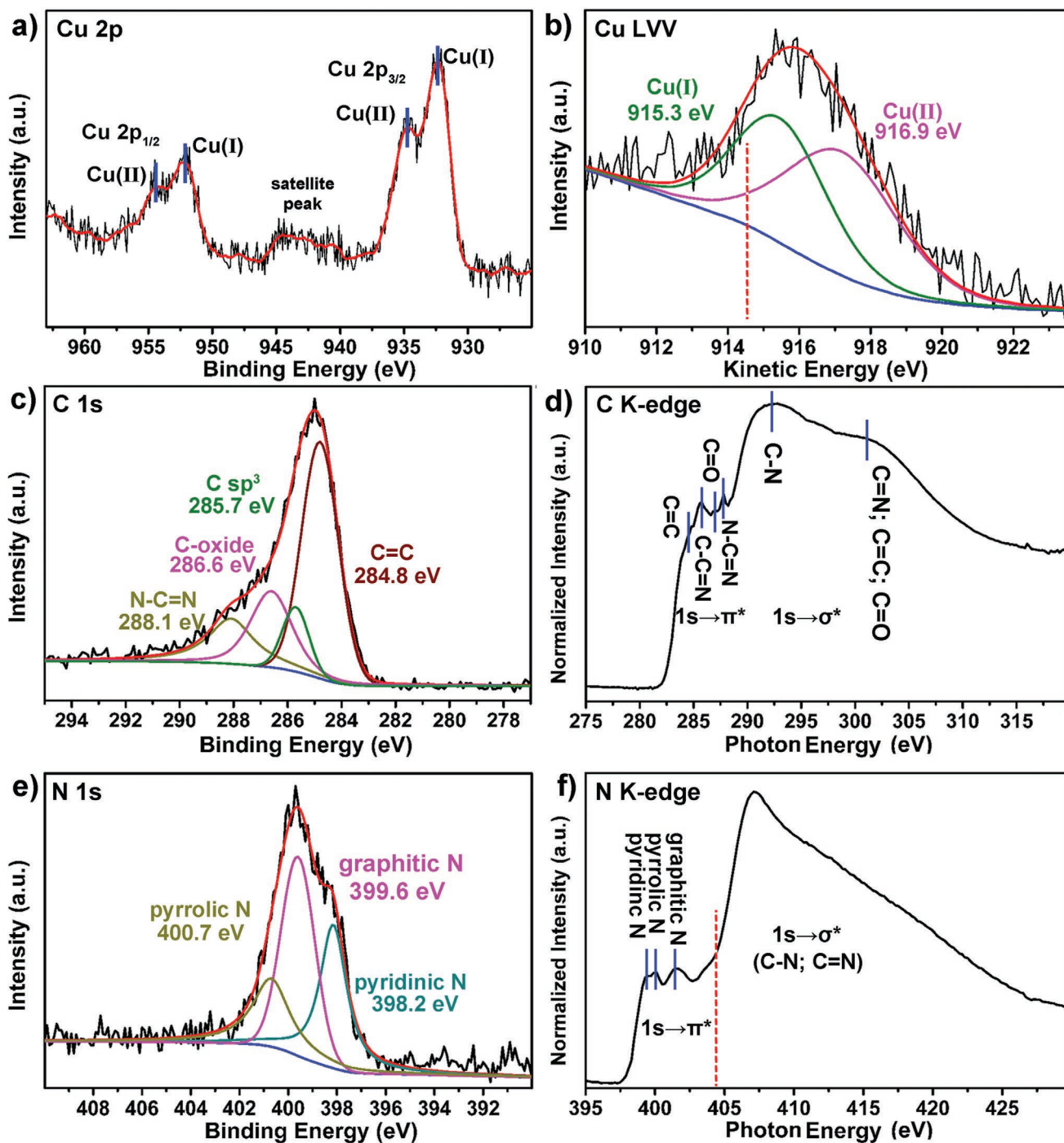


**Figure 2.** XPS and NEXAFS spectra of DAS-Cu. a,b) Cu 2p XPS spectrum and Cu LVV Auger spectrum of DAS-Cu. c,d) C 1s XPS spectrum and C K-edge NEXAFS spectrum of DAS-Cu. e,f) N 1s XPS spectrum and N K-edge NEXAFS spectrum of DAS-Cu.

optimized geometries are listed in Figure 3b. Their relative energies reveal that the energy of the DAS-Cu catalyst increases when the Cu–N<sub>4</sub>/Cu–N<sub>3</sub> distance extends from 5.33 to 9.08 Å (Figure 3c). The result indicates that the dual Cu sites are more likely to locate close to each other. To further certify the stabilities of the proposed structures, the binding energy per Cu atom on the graphene substrate is calculated. Among the 6 types of the Cu–N<sub>4</sub> and Cu–N<sub>3</sub> distributions, the average Cu binding

energy is calculated to be highly exothermic of –1.01 to –1.15 eV, indicating that the isolated Cu–N<sub>4</sub> and Cu–N<sub>3</sub> distributions on the nitrogen doped graphene substrate exhibits high stabilities, and the single Cu sites are less likely to agglomerate (detailed calculation methods and results are shown in Table S2, Supporting Information).

The electronic structure of DAS-Cu is studied using the model with the Cu–Cu distance of 5.33 Å. Its spin density

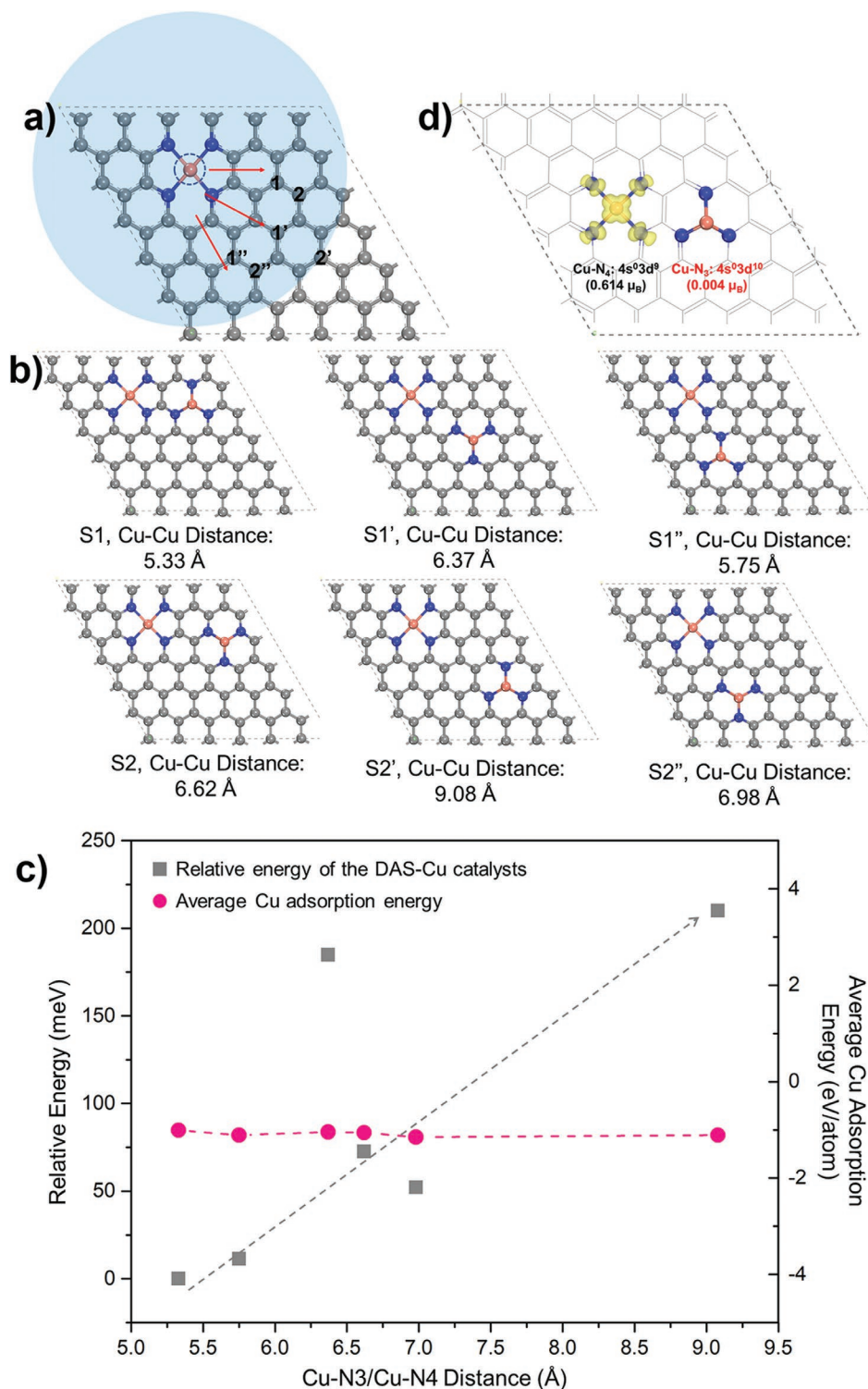


**Figure 3.** DFT calculation. a) Schematic of possible single C vacancy sites for further construction of the Cu-N<sub>3</sub> site. b) The optimized structures of the DAS-Cu surface, with the Cu-N<sub>3</sub> site located in the corresponding C vacancy sites shown in (a). c) The corresponding relative energies and the average Cu binding energies of the DAS-Cu surfaces with different Cu-N<sub>4</sub>/Cu-N<sub>3</sub> dispersion. d) Spin density plot and magnetic moment of the Cu-N<sub>4</sub> and Cu-N<sub>3</sub> site on the DAS-Cu catalyst.

plot is shown in Figure 3d. For the Cu-N<sub>4</sub> site, the Cu atom is anchored on the double carbon vacancy site in the graphene layer and coordinated with four N atoms with the average

Cu-N distance of 1.93 Å. For the Cu-N<sub>3</sub> site, the Cu atom is coordinated with three pyridinic N atoms with the average Cu-N bond length of 1.95 Å, which is in line with the results

in previous report.<sup>[56]</sup> Spin polarized calculations were performed to further illustrate the oxidation state of Cu atoms in DAS-Cu. The magnetic moments of the Cu–N<sub>4</sub> and Cu–N<sub>3</sub> sites are 0.614 and 0.004  $\mu_B$ , respectively (Figure 3d), suggesting the electronic configurations of 4s<sup>0</sup>3d<sup>9</sup> and 4s<sup>0</sup>3d<sup>10</sup> to Cu(II) in Cu–N<sub>4</sub> and Cu(I) in Cu–N<sub>3</sub>, respectively. Additionally, the magnetic moment of Cu atoms in Cu–N<sub>4</sub> site is 0.614  $\mu_B$ , which is close to the value in CuO.<sup>[65,66]</sup> The projected density of states of the Cu–N<sub>3</sub> and Cu–N<sub>4</sub> site is shown in Figure S10 (Supporting Information), which also confirms spin polarization of the Cu–N<sub>4</sub> site.

The oxyphosphorylation reaction of styrene and diethyl phosphite in air is used to evaluate the catalytic activity of DAS-Cu. To our delight, DAS-Cu shows excellent catalytic performance toward the desired product **3aa** in 90% yield (Figure 4). The calculated turnover frequency (TOF) value of the catalyst is 186.4 h<sup>-1</sup>. In contrast, homogeneous Cu catalysts, such as CuBr, CuBr<sub>2</sub>, and Cu(II)-phthalocyanine (possess only Cu–N<sub>4</sub> site) are unreacted under the same condition. SAC-Cu (possess only Cu–N<sub>3</sub> sites; the detailed synthetic procedures are shown in the Experimental Section; Figures S11–S22 and Table S3, Supporting Information) and SAC-Cu-2 (possess only Cu–N<sub>4</sub> sites; synthesized via a reported strategy;<sup>[67]</sup> the detailed synthetic procedures are shown in the Experimental Section; and Figures S23–S25, Supporting Information) were prepared to evaluate the synergistic effect of Cu–N<sub>3</sub> and Cu–N<sub>4</sub> in this reaction. Interestingly, no reaction occurs when SAC-Cu is used and SAC-Cu-2 only exhibits a low yield of 22%, which indicates that the synergistic effect of two Cu catalytic sites plays the key role in the catalytic system. The catalytic properties of DAS-Cu before teaching (DAS-Cu-NPs; the detailed synthetic procedures and characterizations are shown in the Experimental Section; Figure S26–S28, Supporting Information) have also studied, which show the similar activity (86% yield) toward

this reaction under the same condition. Considering single Cu atoms and nanosized Cu coexist in DAS-Cu-NPs, we also test the catalytic performance of nanosized Cu (TEM images are shown in Figure S29, Supporting Information) and the results show that nanosized Cu exhibits only moderate activity (14% yield) toward this reaction under the same condition. These results strongly certified that the synergistic effect of Cu–N<sub>3</sub> and Cu–N<sub>4</sub> is crucial in this reaction. No desired product is detected with the absence of NaHCO<sub>3</sub>, which suggests that the weak alkaline environment is also essential in this reaction. When the reaction is performed under N<sub>2</sub> atmosphere, no reaction arises, which gives evidence that air serves as the oxidant in this reaction system. Moreover, DAS-Cu also shows good recyclability toward the oxyphosphorylation reaction. The characterizations of DAS-Cu after reaction (DAS-Cu-cycled) indicate that DAS-Cu nearly unchanged after reaction (TEM, STEM, XRD, AC-HAADF-STEM, EXAFS, and XPS are shown in Figures S30–S42 and Table S4, Supporting Information). Furthermore, ICP-OES is used to analyze the liquid phase of reaction solution. Only a slight amount of dissolved Cu (Cu: 0.6 ppm; 0.3% of the total Cu atoms in DAS-Cu) is detected, which also demonstrates the good stability of DAS-Cu.

In order to explore the influence of substrate categories, the substrate scope of the oxyphosphorylation reaction is investigated under the same reaction condition. As shown in Figure S43 (Supporting Information), the aromatic alkenes with electro-donating substituents (–Me and –OMe) can react beneficially with diethylphosphite to produce **3ba** and **3ca** at the yield of 93% and 97%, respectively. When styrene derivatives bear electron-withdrawing groups (–F, –Cl, and –AcO), the target products **3da–3fa** are obtained in relatively moderate yields (82–73%). As for 2-vinylnaphthalene using in the reaction, the desired product **3ga** can also be isolated in a yield of 83%. Moreover, DAS-Cu also exhibits good catalytic performance for oxyphosphorylation of internal aryl alkenes ( $\beta$ -methylstyrene), furnishing the target product **3ha** in 80% yield. Besides the different alkenes, different H-phosphonates (diisopropylphosphite and diisobutylphosphite) can also work well with styrene to provide products **3ab** and **3ac** in a good yield of 88% and 77%, respectively.

To investigate the reaction mechanism, EPR technique was performed with 5,5-dimethyl-1-pyrroline N-oxide as spin trapping agents. When the reaction is heated to 80 °C without any catalysts, no signals of radicals are detected. Superoxide radicals can be detected when DAS-Cu added to the reaction system for 3 min. When prolonging the reaction time, the signals of superoxide radicals become more obviously ( $a_H = 10$  G,  $a_N = 13$  G; Figure S44, Supporting Information).<sup>[68]</sup> On the contrary, SAC-Cu shows no detectable signals after 10 min reaction (Figure S45, Supporting Information). These results suggest that the simultaneous existence of Cu–N<sub>3</sub> and Cu–N<sub>4</sub> active sites promotes the formation of superoxide radicals and thus accelerates the reaction.

Previous reports have proposed the reaction mechanisms for homogeneous catalytic alkene oxyphosphorylation to  $\beta$ -ketophosphonate,<sup>[44–46]</sup> in which the activation of O<sub>2</sub> through the Cu(O–O·) superoxide formation is the key step, followed by (RO)<sub>2</sub>P(O)H dehydrogenation and radical formation. In this work, our DFT calculations reveal that the Cu–N<sub>3</sub> site exhibits

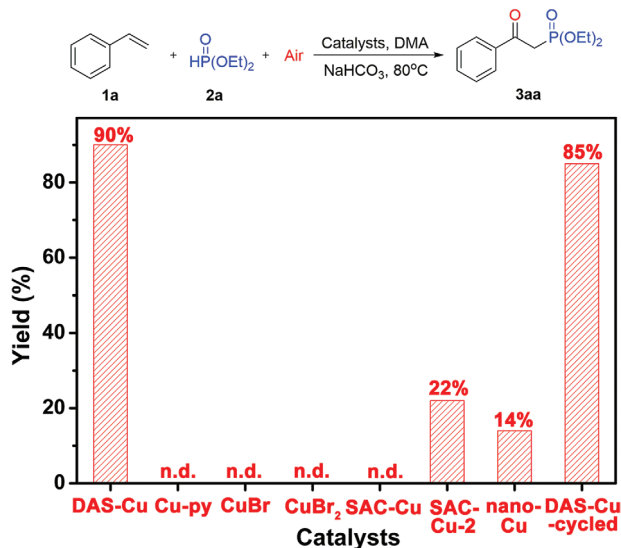


**Figure 4.** Oxyphosphorylation of styrene to form  $\beta$ -ketophosphonate. Unless otherwise noted, all reactions were carried out at a 0.22 mmol scale in DMA (0.5 mL) at 80 °C for 2 h with 2 mg catalysts, a molar ratio of **1a/2a** = 1: 1.1 and 2 mg NaHCO<sub>3</sub>. Yield is determined by gas chromatography equipped with a flame ionization detector with 20  $\mu$ L dodecane as internal standard.

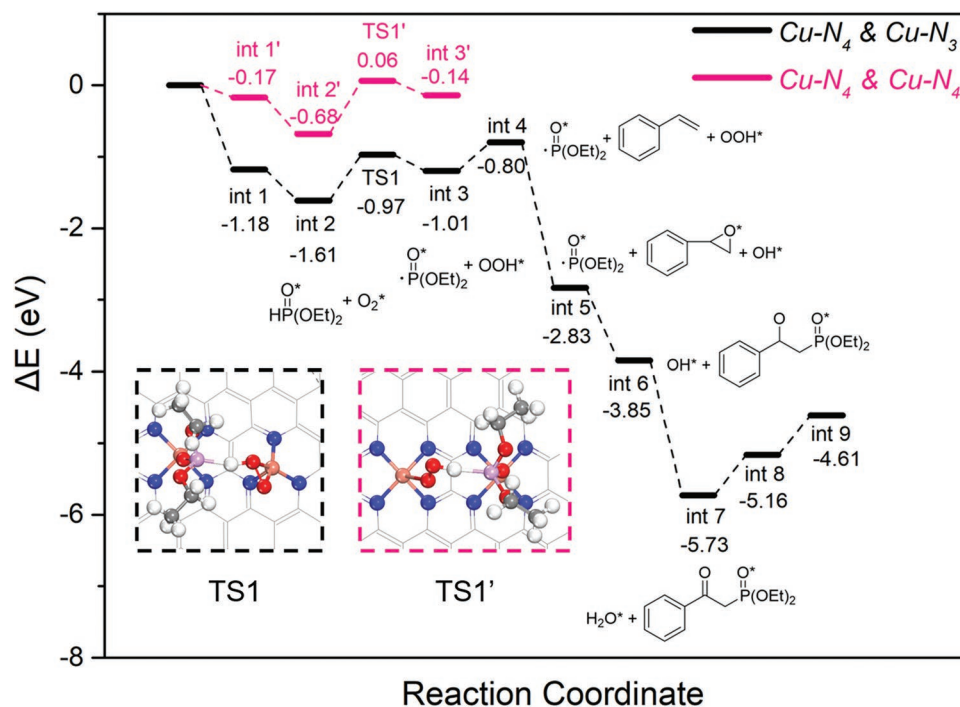


**Figure 5.** Potential energy surfaces for styrene oxyphosphorylation to  $\beta$ -ketophosphonate over DAS-Cu catalyst. The reaction intermediate from each elementary step is represented by int, and detailed structures for all reaction intermediates are shown in Figure S47 (Supporting Information) (H white, C gray, blue N, red O, purple P, orange Cu).

high reactivity toward  $O_2$ , with highly exothermic adsorption energy of  $-1.18$  eV (Figure 5). In contrast,  $O_2$  adsorption on the Cu- $N_4$  site is much less favorable, with the adsorption energy calculated to be  $-0.17$  eV. These results suggest that Cu- $N_3$  sites in DAS-Cu can capture the gaseous  $O_2$  more effectively and trigger the subsequent diethyl phosphite dehydrogenation. To certify this result,  $O_2$  temperature-programmed desorption ( $O_2$ -TPD) experiments of DAS-Cu with SACs-Cu-2 as references have been carried out. We can see the only peak at  $\approx 160$  °C in the plots of SAC-Cu-2, indicating that the  $O_2$  physical adsorption is dominant on the surface of SAC-Cu-2 (Figure S46, Supporting Information). However, the main signal appears at above 200 °C, which suggests that  $O_2$  strongly adsorbs on the surface of DAS-Cu. These results are in good consistent with our previous results and strongly illustrate that Cu- $N_3$  sites are regarded to account for  $O_2$  activation. Upon  $O_2$  chemisorption on the Cu- $N_3$  site, the Cu atom in the adjacent Cu- $N_4$  further provides the adsorption site for diethyl phosphite and the PO-Cu bond length is 2.41 Å (Figure S47, int 2, Supporting Information) with the exothermic adsorption energy of  $-0.43$  eV. The adsorbed diethyl phosphite can further react with the  $O_2^*$  to form the  $OOH^*$  and the phosphonyl radical ( $\cdot PO(OEt)_2$ ) intermediate (Figure S47, int 3, Supporting Information), with the reaction energy and the energy barrier of 0.60 and 0.64 eV, respectively. Same reaction pathway on SAC-Cu catalyst with two Cu- $N_4$  sites was also calculated for comparison (Figure 5). The adsorption energy of diethyl phosphite on the Cu- $N_4$  site is calculated to be  $-0.51$  eV. Cu- $N_4$ - $O_2^*$  species on SAC-Cu surface are less reactive than the Cu- $N_3$ - $O_2^*$  species on DAS-Cu surface, with the diethyl phosphite dehydrogenation energy barrier and reaction energy of 0.74 and

0.54 eV, respectively. The above calculations reveal the Cu(I) in the Cu- $N_3$  site have higher reducibility and reactivity toward oxide species ( $O_2$ , diethyl phosphite, and phosphonyl radical). Spin density plots of phosphonyl species locating at the Cu- $N_3$  and Cu- $N_4$  sites are shown in Figure S48 (Supporting Information) with the magnetic moment of the P atom 0.02  $\mu_B$  for the former and 0.14  $\mu_B$  for the latter, respectively, indicating that the dehydrogenated diethyl phosphite still remains the feature of a radical when adsorbing on the Cu- $N_4$  site. From the above data, it can be concluded that the Cu- $N_3$  site is mainly responsible for capturing  $O_2$  in the gas phase, while the Cu- $N_4$  is the moderate adsorption site for diethyl phosphite and can effectively protect the phosphonyl radical.

After the formation of the phosphonyl radical, the physisorbed styrene can be easily oxidized by the  $OOH^*$  on the adjacent Cu- $N_3$  site to form styrene oxide (int 5), which is highly exothermic with the reaction energy of  $-2.03$  eV. Meanwhile, we have also investigated the alternative reaction pathway of phosphonyl radical direct coupling with the styrene (Figure S49, Supporting Information), and the reaction energy of this step is  $-1.11$  eV, which demonstrate that the former reaction pathway is more favorable. The generated styrene oxide further couples with the phosphonyl radical (Figure S47, int 6, Supporting Information), and the reaction energy is  $-1.02$  eV. On the other hand, the reaction is much less favorable on the SAC-Cu surface exposing two Cu- $N_3$  sites due to the strong interaction between  $PO(OEt)_2$  and Cu- $N_3$ , in which the radical structure is destroyed, and the reaction energy is  $-0.21$  eV (Figure S50, Supporting Information). After the coupling of  $\cdot PO(OEt)_2$  and styrene oxide, the H atom further transfers to the  $OH^*$  to generate the target product ( $\beta$ -ketophosphonate) and  $H_2O$  with

the reaction energy of  $-1.88$  eV. The catalyst can be regenerated with the desorption of  $\beta$ -ketophosphonate and  $H_2O$ . In conclusion, three key elementary steps are involved in total: oxidation of styrene, styrene oxide coupling with phosphonyl radical, and hydrogen transfer to form  $\beta$ -ketophosphonate. All of these reaction steps are thermodynamically favorable, which explains the high reactivity of the DAS-Cu catalyst to the target products.

### 3. Conclusion

In conclusion, we report a facile method to prepare DAS-Cu catalysts by pyrolyzing Cu complexes with Cu atoms in different coordination sphere. DAS-Cu shows robust activity (up to yields: 97% in 2 h reaction) toward oxyphosphorylation of styrene and its derivatives. The high activity of atomically dispersed Cu-N<sub>3</sub> and Cu-N<sub>4</sub> sites are responsible chiefly for the terrific catalytic properties. DFT calculations revealed the synergistic effect of two different Cu sites in DAS-Cu toward styrene oxyphosphorylation: Cu-N<sub>3</sub> sites capture the oxygen and trigger further oxidizing reactions, Cu-N<sub>4</sub> sites stabilize the reactant via moderate adsorption and protect the phosphonyl radical. Overall, this work not only provides a novel strategy to prepare dual-active sites Cu catalysts but also points out a new way for potential applications of such catalysts.

### 4. Experimental Section

**The Preparation of DAS-Cu:** In a typical synthetic procedure of DAS-Cu, creatine (6.00 g; 45.8 mmol) and  $Cu(NO_3)_2 \cdot 2.5 H_2O$  (1.331 g; 5.72 mmol; 0.125 eq) were first added to a flask containing 25 mL deionized water with vigorously stirring at 80 °C. After stirring for 2 h, sodium hydroxide (1.83 g; 45.8 mmol) was added to the slight yellow solution and raise the temperature to 100 °C to evaporate water and ensure the completion of coordination for 24 h. The collected claret red solid ( $\approx 8.4$  g with reasonable losses) was placed in a tube furnace and then heated to 600 °C for 2 h at the heating rate of 5 °C min<sup>-1</sup> under flowing Ar gas, heated under mixed gas (hydrogen 5% in Ar) to 400 °C for 2 h and then naturally cooled to room temperature to obtain the representative samples (2.89 g, pyrolyzed loss rate 65.5%). The obtained sample was washed with deionized water for three times to remove soluble impurities (denoted as DAS-Cu-NPs; 0.80 g; nominal loading: 45.4 wt%; actual loading: 40.2 wt%). Cu NPs was etched with saturate  $CuSO_4$  in HCl solution (35 wt%) and finally catalysts were obtained (0.45 g; nominal loading: 2.9 wt%; actual loading: 4.6 wt%).

**The Preparation of SAC-Cu:** Guanidine thiocyanate (6 g; 50.8 mmol) and  $Cu(NO_3)_2 \cdot 2.5 H_2O$  (1.452 g; 6.35 mmol; 0.125 eq) were added to a flask containing 25 mL deionized water with vigorously stirring at 80 °C. After stirring for 2 h, raise the temperature to 100 °C to evaporate water and ensure the completion of coordination for 24 h. The collected brown solid ( $\approx 7$  g with reasonable losses) was placed in a tube furnace and then heated to 600 °C for 2 h at the heating rate of 5 °C min<sup>-1</sup> under flowing Ar gas, heated under mixed gas (hydrogen 5% in Ar) to 400 °C for 2 h and then naturally cooled to room temperature to obtain the representative samples (1.4 g, pyrolyzed loss rate 80%). The obtained sample was washed with water and ethanol for three times and SAC-Cu is obtained ( $\approx 1.35$  g).

**The Preparation of SAC-Cu-2:** SAC-Cu-2 is prepared via a reported strategy.<sup>[67]</sup> 2-methylimidazole (2.63 g) was dissolved in methanol (40 mL; solution A).  $Zn(NO_3)_2 \cdot 6H_2O$  (2.38 g). and  $Cu(CH_3COO)_2 \cdot H_2O$  (0.16 g), were dissolved in methanol (60 mL; solution B). After

vigorous stirring for 10 min, solution B was poured into solution A and the mixed solution was stirred for 30 min. Subsequently, the mixture was transferred into 100 mL Teflon-lined autoclave and heated at 120 °C for 4 h. The products were washed with methanol and *N,N*-dimethylformamide, respectively, for three times and dried at 60 °C for whole night. The obtained powders were pyrolyzed at 1000 °C for 4 h under nitrogen atmosphere. The heating rate was set to 5 °C min<sup>-1</sup>. The as-obtained black powder is SAC-Cu-2 ( $\approx 45$  mg).

**The Preparation of Nanosized Cu:** At first, Vulcan XC-72 (100 mg), polyvinyl pyrrolidone (K30, 100 mg), and  $Cu(NO_3)_3 \cdot 3H_2O$  (38 mg; nominal loading: 10 wt%) was ultrasonically dispersed in deionized water (20 mL) at room temperature.  $NaBH_4$  (12.8 mg; 4 eq) in 20 mL deionized water was added dropwise to  $Cu(NO_3)_2$  solution. After stirred continuously for 2 h, black powders were collected by centrifugation and washed by deionized water and ethanol twice, respectively. The as-obtained nanosized Cu catalyst was dried at 70 °C for 12 h to remove the solvent, then the solid was used for catalytic tests without further purification.

**Catalytic Tests for Oxyphosphorylation Reaction:** In a typical procedure, styrene (or its derivatives; 0.22 mmol), diethyl phosphate (0.24 mmol; 1.1 eq),  $NaHCO_3$  (2 mg), DAS-Cu catalysts (2 mg, Cu/substrate = 0.6 mol%) and *N,N*-dimethylacetamide (DMA) (0.5 mL) were first added to a Shlenck tube equipped with a stir bar, and the mixture was stirred at 80 °C for 2 h. After the reaction finished, the reaction mixture was analyzed by gas chromatography equipped with a flame ionization detector and gas chromatography-mass spectrometry with dodecane as the internal standard. The crude reaction mixture was purified by extraction with saturated NaCl solution and flash chromatography on silicone gel (eluent: hexane/ethyl acetate, v/v = 3/1) to afford corresponding products. The overall TOF value was measured upon completion of reactions and the calculation of it was based on the total Cu loading in the catalyst.

**Catalyst Recycling Test:** After the reaction finished, the reaction mixture was centrifuged and the liquid layer was siphoned out. DAS-Cu was washed with ethyl acetate, ethanol, and deionized water three times, respectively. The black solid was collected by centrifugation and was dried in a vacuum over 40 °C for 8 h. Finally, the recovered DAS-Cu was used in the subsequent reaction without further purification.

### Supporting Information

Supporting Information is available from the Wiley Online Library or from the author.

### Acknowledgements

Y.X. and S.W. contributed equally to this work. This work was supported by the National Key R&D Program of China (No. 2018YFA0702003), the National Natural Science Foundation of China (Nos. 21890383 and 21871159), Science and Technology Key Project of Guangdong Province of China (No. 2020B010188002), and China Postdoctoral Science Foundation (Nos. 2018M640114 and 2019M650626). The authors thank the BL14W1 station in Shanghai Synchrotron Radiation Facility (SSRF) and 1W1B station for XAFS measurement in Beijing Synchrotron Radiation Facility (BSRF). They also appreciate the BL12B station of National Synchrotron Radiation Laboratory (NRS) for NEXAFS measurement. They appreciate Ningqiang Zhang for providing O<sub>2</sub>-TPD test and Yunhu Han for taking TEM images.

### Conflict of Interest

The authors declare no conflict of interest.

## Data Availability Statement

Data sharing is not applicable to this article as no new data were created or analyzed in this study.

## Keywords

dual-active-site catalysts, oxyphosphorylation reaction, single atom catalysts

Received: November 1, 2020

Revised: December 31, 2020

Published online: February 1, 2021

- [1] H. S. Taylor, *Proc. R. Soc. London, Ser. A* **1925**, 108, 105.
- [2] M. Boudart, *Adv. Catal.* **1969**, 20, 153.
- [3] L. Liu, A. Corma, *Chem. Rev.* **2018**, 118, 4981.
- [4] L. Ma, G. Zhu, D. Wang, H. Chen, Y. Lv, Y. Zhang, X. He, H. Pang, *Adv. Funct. Mater.* **2020**, 30, 2003870.
- [5] J. Yang, W. Li, D. Wang, Y. Li, *Small Struct.* **2020**, <https://doi.org/10.1002/sstr.202000051>.
- [6] Q. Chen, Y. Jia, S. Xie, Z. Xie, *Chem. Soc. Rev.* **2016**, 45, 3207.
- [7] Y. Yamada, C. Tsung, W. Huang, *Nat. Chem.* **2011**, 3, 372.
- [8] Y. Li, W. Shen, *Chem. Soc. Rev.* **2014**, 43, 1543.
- [9] L. Huang, M. Liu, H. Lin, Y. Xu, J. Wu, V. P. Dravid, C. Wolverton, C. A. Mirkin, *Science* **2019**, 365, 1159.
- [10] B. H. Lee, S. Park, M. Kim, A. K. Sinha, S. C. Lee, E. Jung, W. J. Chang, K. S. Lee, J. H. Kim, S. P. Cho, H. Kim, K. T. Nam, T. Hyeon, *Nat. Mater.* **2019**, 18, 620.
- [11] K. Murugesan, V. G. Chandrashekar, T. Senthamarai, R. V. Jagadeesh, M. Beller, *Nat. Protoc.* **2020**, 15, 1313.
- [12] A. Wang, J. Li, T. Zhang, *Nat. Rev. Chem.* **2018**, 2, 65.
- [13] B. Q. Li, C. X. Zhao, S. Chen, J. N. Liu, X. Chen, L. Song, Q. Zhang, *Adv. Mater.* **2019**, 31, 1900592.
- [14] H. Xu, D. Cheng, D. Cao, X. C. Zeng, *Nat. Catal.* **2018**, 1, 339.
- [15] C. Zhu, S. Fu, Q. Shi, D. Du, Y. Lin, *Angew. Chem., Int. Ed.* **2017**, 56, 13944.
- [16] J. Liu, *ACS Catal.* **2017**, 7, 34.
- [17] E. D. Goodman, A. C. Johnston-Peck, E. M. Dietze, C. J. Wrasman, A. S. Hoffma, F. Abild-Pedersen, S. R. Bare, P. N. Plessow, M. Cargnello, *Nat. Catal.* **2019**, 2, 748.
- [18] M. D. Marcinkowski, M. T. Darby, J. Liu, J. M. Wimple, F. R. Lucci, S. Lee, A. Michaelides, M. Flytzani-Stephanopoulos, M. Stamatakis, E. C. H. Sykes, *Nat. Chem.* **2018**, 10, 325.
- [19] J. Han, X. Meng, L. Lu, J. Bian, Z. Li, C. Sun, *Adv. Funct. Mater.* **2019**, 10, 1808872.
- [20] A. Bakandritsos, R. G. Kadam, P. Kumar, G. Zoppellaro, M. Medved', J. Tuček, T. Montini, O. Tomanec, P. Andrášková, B. Drahoš, R. S. Varma, M. Otyepka, M. B., P. F. Gawande, R. Zbořil, *Adv. Mater.* **2019**, 31, 1900323.
- [21] H. H. Ou, D. S. Wang, Y. D. Li, *Nano Select* **2020**, <https://doi.org/10.1002/nano.202000239>.
- [22] N. Zhang, C. Ye, H. Yan, L. Li, H. He, D. Wang, Y. Li, *Nano Res.* **2020**, 13, 3165.
- [23] X. Li, H. Rong, J. Zhang, D. Wang, Y. Li, *Nano Res.* **2020**, 13, 1842.
- [24] J. Liu, *Chin. J. Catal.* **2017**, 38, 1460.
- [25] S. Tian, M. Hu, Q. Xu, W. Gong, W. Chen, J. Yang, Y. Zhu, C. Chen, J. He, Q. Liu, H. Zhao, D. Wang, Y. Li, *Sci. China Mater.* **2020**, <https://doi.org/10.1007/s40843-020-1443-8>.
- [26] Z. Zhuang, Q. Kang, D. Wang, Y. Li, *Nano Res.* **2020**, 13, 1856.
- [27] S. Lin, C. S. Diercks, Y. B. Zhang, N. Kornienko, E. M. Nichols, Y. Zhao, A. R. Paris, D. Kim, P. Yang, O. M. Yaghi, C. J. Chang, *Science* **2015**, 349, 1208.
- [28] J. Yang, W. Li, D. Wang, Y. Li, *Adv. Mater.* **2020**, 32, 2003300.
- [29] T. Sun, L. Xu, D. Wang, Y. Li, *Nano Res.* **2019**, 12, 2067.
- [30] S. H. Ahn, A. Manthiram, *Small* **2020**, 16, 2002511.
- [31] W. Xiong, H. Li, H. Wang, J. Yi, H. You, S. Zhang, Y. Hou, M. Cao, T. Zhang, R. Cao, *Small* **2020**, 16, 2003943.
- [32] M. Fan, J. Cui, J. Wu, R. Vajtai, D. Sun, P. M. Ajayan, *Small* **2020**, 16, 1906782.
- [33] Z. Chen, E. Vorobyeva, S. Mitchell, E. Fako, M. A. Ortuño, N. López, S. M. Collins, P. A. Midgley, S. Richard, G. Vilé, J. Pérez-Ramírez, *Nat. Nanotechnol.* **2018**, 13, 702.
- [34] Z. Lu, B. Wang, Y. Hu, W. Liu, Y. Zhao, R. Yang, Z. Li, J. Luo, B. Chi, Z. Jiang, M. Li, S. Mu, S. Liao, J. Zhang, X. Sun, *Angew. Chem., Int. Ed.* **2019**, 58, 2622.
- [35] K. Kratzl, T. Kratky, S. Günther, O. Tomanec, R. Zbořil, J. Michalička, J. M. Macak, M. Cokoja, R. A. Fischer, *J. Am. Chem. Soc.* **2019**, 141, 13962.
- [36] J. Kim, H.-E. Kim, H. Lee, *ChemSusChem* **2018**, 11, 104.
- [37] R. Zhao, Z. Liang, S. Gao, C. Y., B. Zhu, J. Zhao, C. Qu, R. Zou, Q. Xu, *Angew. Chem., Int. Ed.* **2019**, 131, 1997.
- [38] E. Vorobyeva, E. Fako, Z. Chen, S. M. Collins, D. Johnstone, P. A. Midgley, R. Hauert, O. V. Safonova, G. Vil, N. Lopez, S. Mitchell, J. Pérez-Ramírez, *Angew. Chem., Int. Ed.* **2019**, 58, 8724.
- [39] M. Xiao, Y. Chen, J. Zhu, H. Zhang, X. Zhao, L. Gao, X. Wang, J. Zhao, J. Ge, Z. Jiang, S. Chen, C. Liu, W. Xing, *J. Am. Chem. Soc.* **2019**, 141, 17763.
- [40] M. B. Gawande, P. Fornasiero, R. Zboril, *ACS Catal.* **2020**, 10, 2231.
- [41] S. Yuan, L. L. Cui, Z. Dou, X. Ge, X. He, W. Zhang, T. Asefa, *Small* **2020**, 16, 2000742.
- [42] W. S. Wadsworth, W. D. Emmons, *J. Am. Chem. Soc.* **1961**, 83, 1733.
- [43] J. Boutagy, R. Thomas, *Chem. Rev.* **1974**, 74, 87.
- [44] W. Wei, J. X. Ji, *Angew. Chem., Int. Ed.* **2011**, 50, 9097.
- [45] J. Gu, C. Cai, *Org. Biomol. Chem.* **2017**, 15, 4226.
- [46] X. Chen, X. Chen, X. Li, C. Qu, L. Qu, W. Bi, K. Sun, Y. Zhao, *Tetrahedron* **2017**, 73, 2439.
- [47] Y. Cheng, S. Zhao, B. Johannessen, J. P. Veder, M. Saunders, M. R. Rowles, M. Cheng, C. Liu, M. F. Chisholm, R. D. Marco, H. M. Cheng, S. Z. Yang, S. P. Jiang, *Adv. Mater.* **2018**, 30, 1706287.
- [48] X. Fang, Q. Shang, Y. Wang, L. Jiao, T. Yao, Y. Li, Q. Zhang, Y. Luo, H. L. Jiang, *Adv. Mater.* **2018**, 30, 1705112.
- [49] T. Zhang, D. Zhang, X. Han, T. Dong, X. Guo, C. Song, R. Si, W. Liu, Y. Liu, Z. Zhao, *J. Am. Chem. Soc.* **2018**, 140, 16936.
- [50] S. Carniato, G. Dufour, Y. Luo, H. Ågren, *Phys. Rev. B* **2002**, 66, 045105.
- [51] Y. Bu, C. J. Weststrate, J. W. Niemantsverdriet, O. A. Fredriksson, *ACS Catal.* **2016**, 6, 7994.
- [52] D. Atzei, M. Fantauzzi, A. Rossi, P. Fermo, A. Piazzalunga, G. Valli, R. Vecchi, *Appl. Surf. Sci.* **2014**, 307, 120.
- [53] B. Yan, D. Liu, X. Feng, M. Shao, Y. Zhang, *Adv. Funct. Mater.* **2020**, 30, 2003007.
- [54] K. Mudiyansele, A. K. Burrell, S. D. Senanayake, H. Idriss, *Surf. Sci.* **2019**, 680, 107.
- [55] J. Zhang, C. Zheng, M. Zhang, Y. Qiu, Q. Xu, W. C. Cheong, W. Chen, L. Zheng, L. Gu, Z. Hu, D. Wang, Y. Li, *Nano Res.* **2020**, 13, 3082.
- [56] K. G. Latham, M. I. Simone, W. M. Dose, J. A. Allen, S. W. Donne, *Carbon* **2017**, 114, 566.
- [57] R. Bertoncello, M. Bettinelli, M. Casarin, A. Gulino, E. Tondello, A. Vittadini, *Inorg. Chem.* **1992**, 31, 1558.
- [58] A. Zitolo, V. Goellner, V. Armel, M. T. Sougrati, T. Mineva, L. Stievano, E. Fonda, F. Jaouen, *Nat. Mater.* **2015**, 14, 937.
- [59] H. T. Chung, D. A. Cullen, D. Higgins, B. T. Sneed, E. F. Holby, K. L. More, P. Zelenay, *Science* **2017**, 357, 479.

- [60] J. Liu, X. Sun, P. Song, Y. Zhang, W. Xing, W. Xu, *Adv. Mater.* **2013**, *25*, 6879.
- [61] J. Liu, M. Jiao, L. Lu, H. M. Barkholtz, Y. Li, Y. Wang, L. Jiang, Z. Wu, D. J. Liu, L. Zhuang, C. Ma, J. Zeng, B. Zhang, D. Su, P. Song, W. Xing, W. Xu, Y. Wang, Z. Jiang, G. Sun, *Nat. Commun.* **2017**, *8*, 15938.
- [62] W. Yang, S. Xu, K. Ma, C. Wu, I. D. Gates, X. Ding, W. Meng, Z. Gao, *Nano Mater. Sci.* **2020**, *2*, 120.
- [63] W. Li, C. Min, F. Tan, Z. Li, B. Zhang, R. Si, M. Xu, W. Liu, L. Zhou, Q. Wei, Y. Zhang, X. Yang, *ACS Nano* **2019**, *13*, 3177.
- [64] Z. Yang, B. Chen, W. Chen, Y. Qu, F. Zhou, C. Zhao, Q. Xu, Q. Zhang, X. Duan, Y. Wu, *Nat. Commun.* **2019**, *10*, 3734.
- [65] A. K. Mishra, A. Roldan, N. H. de Leeuw, *J. Phys. Chem. C* **2016**, *120*, 2198.
- [66] B. X. Yang, T. R. Thurston, J. M. Tranquada, G. Shirane, *Phys. Rev. B: Condens. Matter Mater. Phys.* **1989**, *39*, 4343.
- [67] K. Zhao, X. Nie, H. Wang, S. Chen, X. Quan, H. Yu, W. Choi, G. Zhang, B. Kim, J. G. Chen, *Nat. Commun.* **2020**, *11*, 2455.
- [68] G. M. Rosen, E. J. Rauckman, *Mol. Pharmacol.* **1980**, *17*, 233.